The Astrophysical Journal Letters, 940:L21 (8pp), 2022 November 20 https://doi.org/10.3847/2041-8213/ac9f37

The Emission Properties of RRAT J0139+3336 at 1.25 GHz

Jintao Xie[1,2], Jingbo Wang[3,4,5], Na Wang[1,4,5], Feifei Kou[1,4,5], Shuangqiang Wang[1], and Shengnan Sun[1,2]
[1] Xinjiang Astronomical Observatory, Chinese Academy of Sciences, Urumqi, Xinjiang 830011, People's Republic of China; 1983wangjingbo@163.com, na.wang@xao.ac.cn
[2] University of Chinese Academy of Sciences, Beijing 100049, People's Republic of China
[3] Institute of Optoelectronic Technology, Lishui University, Lishui, Zhejiang, 323000, People's Republic of China
[4] Key Laboratory of Radio Astronomy, Chinese Academy of Sciences, Urumqi, Xinjiang, 830011, People's Republic of China
[5] Xinjiang Key Laboratory of Radio Astrophysics, Urumqi, Xinjiang, 830011, People's Republic of China
Received 2022 August 17; revised 2022 November 2; accepted 2022 November 2; published 2022 November 21

Abstract

Rotating Radio Transients are a relatively new subclass of pulsar characterized by sporadic bursting emission of single pulses. Here, we present a single-pulse analysis of a rotating radio transient, RRAT J0139+3336, using Five-hundred-meter Aperture Spherical radio Telescope at 1250 MHz. Within 3.32 hr of continuous observation, 152 single pulses were detected in RRAT J0139+3336, with the pulse rate of 45 pulses per hour. We perform a spectral analysis on the single pulses of this pulsar for the first time, finding its mean spectral indices to be -3.2 ± 0.2, which is steeper than most known pulsars. On a single-pulse basis, we produce the first polarimetric profile of this pulsar, which fits well with the rotating vector model. The single pulses are clearly affected by diffractive scintillation with a characteristic scintillation bandwidth of $\nu_{sc} = 28 \pm 9$ MHz. The pulse energy distribution for RRAT J0139+3336 can be described by a log-normal model.

Unified Astronomy Thesaurus concepts: Radio pulsars (1353)

1. Introduction

Rotating Radio Transients (RRATs) are a relatively new subclass of the pulsar, which were first discovered by reprocessing the Parkes Multi-beam Pulsar Survey for single-pulse searches (McLaughlin et al. 2006). RRATs are characterized by sporadic emission of single pulses, where an individual pulse is detected followed by no detectable emission for many pulse periods (sometimes minutes to hours). RRATs are Galactic pulsars with extreme emission variability (McLaughlin et al. 2009). The expected single-pulse rates of RRATs are in the range of several pulses to several hundred pulses per hour. Consequently, they are more likely to be detected by single-pulse searches as against the standard Fourier domain search or conventional folding techniques.

The mean magnetic fields and period derivatives of RRATs are higher than those of normal pulsars (Cui et al. 2017). Other properties of RRATs, such as pulse width distributions, and Galactic z-distribution, are similar to those of normal pulsars (Burke-Spolaor & Bailes 2010). Currently, there are more than 120 known RRATs.[6] The physics responsible for the sporadic nature of the emission, nevertheless, remains poorly understood. Several models have been proposed to explain the cause of the sporadic emission from RRATs. These models include interference of an asteroid belt around a pulsar (Cordes & Shannon 2008), the fallback of material from a supernova debris disk (Li 2006), or mechanisms within the pulsar magnetosphere (e.g., Timokhin 2010; Melrose & Yuen 2014). Alternatively, RRATs may be normal pulsars that exhibit extreme nulling (Wang et al. 2007).

The properties of pulsar radiation can be constrained with polarimetric measurements (Rookyard et al. 2015). The analysis of the polarization characteristics is made challenging by the nature of the sporadic radiation of the RRATs, which makes it difficult to define the integral profile. However, they could still furnish significant insight into the nature of the emission even though they are on the basis of a small number of single pulses. It is unclear whether the RRAT population exhibits polarization characteristics like those of the normal pulsar population. This is partly due to the difficulty of creating high-quality polarimetric profiles of RRATs. It is also useful to understand the emission mechanisms of RRATs and their association with typical pulsar populations through an analysis of the pulse energy distribution since it is a useful tool for a comparison of different pulsar emission modes. The energy distribution of most pulsars is well described by a log-normal distribution (Burke-Spolaor et al. 2012). The so-called giant pulses with power-law energy distributions are considered to be generated separately from standard pulse generation (Cordes et al. 2004; Karuppusamy et al. 2010).

RRAT J0139+3336, also known as J0139+33, was first detected at 111 MHz by the Big Scanning Antenna of the Pushchino Radio Astronomy Observatory (Samodurov et al. 2017) and later identified as an RRAT (Tyul'bashev et al. 2018). It has a long spin period of 1.24 s, a period derivative of 2.06×10^{-15} s s^{-1}, which implies a characteristic age of 10 Myr and a moderate dispersion measure; DM = 21.23 cm^{-3} pc (Sanidas et al. 2019). Michilli et al. (2020) reported the pulse rates of one pulse every ~5 minutes for the multifrequency observations of RRAT J0139+3336 (149 and 1532 MHz with LOFAR and the Lovell telescope), with a distribution roughly consistent with a Poisson distribution. Brylyakova & Tyul'bashev (2021) discovered the existence of giant pulses in RRAT J0139+3336 by analyzing its energy distribution at 111 MHz. Also, the peak flux density in the burst state has a broken power-law distribution in units of S/N.

In this Letter, we present observations of single pulses from RRAT J0139+3336 with the Five-hundred-meter Aperture Spherical radio Telescope (FAST) at a center frequency of 1250 MHz. We investigated the properties of spectral indices

[6] http://astro.phys.wvu.edu/rratalog/

Table 1
Observing Details for FAST on 2020 January 17

Parameter	
Telescope	FAST
Center frequency (MHz)	1250
Bandwidth (MHz)	500
Channel bandwidth (MHz)	0.122
Time resolution (ms)	0.15
UTC Start time	09:38:03
Observation duration (s)	11976

of J0319+3336 and studied its energy distribution and pulse width using the FAST radio telescope. In Section 2, we present the observations and data processing procedures. The analysis and results are presented in Section 3. Discussions and concluding remarks are given in Section 4.

2. Observation and Data Reduction

FAST is a 500 m spherical telescope located in the Guizhou province of China. The aperture of FAST is 500 m, of which 300 m is effective. During observation, the shape of the illuminated area of the reflector is changed into a 300 m aperture paraboloid to realize the main focus antenna. RRAT J0139+3336 was observed with FAST on 2020 January 17 for 3.32 hr. The central beam of the 19-beam receiver with a frequency range from 1 GHz to 1.5 GHz was used (Jiang et al. 2020). The output data were recorded using the Reconfigurable Open Architecture Computing Hardware version 2 (ROACH2) backend with a 122 kHz channel bandwidth and time resolution of 49.152 μs. The data are recorded as an 8-bit sample in polarimetric search mode PSRFITS format. Details of the observation are listed in Table 1.

The DSPSR software package (van Straten & Bailes 2011) was used to subdivide the data into single-pulse time series' with 8192 phase bins within the full pulse period and to remove interchannel dispersion delays caused by the interstellar medium, and that were incoherently dedispersed using the cataloged DM (21.52 pc cm^{-3}). The ephemeris of the pulsar was obtained from Michilli et al. (2020). The PSRCHIVE routine PAZ (Hotan et al. 2004) was used to eliminate narrowband and impulsive radio frequency interference (RFI). Flux density calibration was made through the observation of the radio galaxy 3C286 (Baars et al. 1977), where the calibration method referred to the description in Liu & Yu (2020). Polarization calibration was implemented by injecting a noise diode signal into the feed (Feng et al. 2021). Calibration solutions were obtained and applied using PSRCHIVE routine PAC.

We used the PSRCHIVE routine RMFIT to determine the rotation measure (RM), resulting in 39.2 ± 0.3 rad m^{-2}. The Faraday rotation from the Earth's ionosphere is 0.59 ± 0.02 rad m^{-2}, which is computed using ionFR (Sotomayor-Beltran et al. 2013). After ionospheric correction, the Faraday rotation originating from the interstellar medium is $\mathrm{RM_{ISM}} = 38.61 \pm 0.32$ rad m^{-2}.

3. Analysis and Results

To identify single pulses from the RRAT, we used the approach described in Wang et al. (2007). In general, a single-pulse phase can be divided into two parts: the pulse region and the off-pulsed region, and the off-pulse energy can usually be described with a Gaussian distribution. The detection threshold was taken as five times the rms of the off-pulse region, The frequency-phase plots of these pulses have been examined carefully to rule out possible RFI. A total of 152 single pulses were detected during 3.32 hr of observation.

Once all single pulses had been identified, a template profile was fitted to each pulse using the least-squares minimization approach with the LEASTSQ function in the PYTHON package SCIPY.[7] A profile template contains up to three Gaussian components for every single pulse, allowing for illustrating the small-scale structure of the variation across the pulse profile. The pulse profile summed over frequency is described by

$$S_{\mathrm{t}} = \sum_{i=1}^{3} A_i \exp\left(-\frac{(t - t_{\mathrm{p}i})^2}{2\sigma_i^2}\right), \quad (1)$$

where S_{t} is flux density at the time of pulses t, i is the ith Gaussian components of the pulse, $t_{\mathrm{p}i}$ is the time of pulse peak of the ith profile components, and σ_i is the component width. Since some of the pulses are weak, there is a baseline noise affecting the fit of these pulses. With the aim of avoiding fit noise, a second or third Gaussian component will be added to the pulse template if reduced chi-squared is at least 20% better than a fit with fewer components. The 20% of reduced chi-squared improvement was determined by a Monte Carlo simulation; 49%, 26%, and 25% of pulses require 1, 2, or 3 Gaussian components in the fit, respectively. The template of each pulse will be used to calculate the pulse width and define the on-pulse region. A number of examples of fitted single-pulse templates are diagrammed in Figure 1.

3.1. Scintillation Bandwidth

It is clear from Figure 1 that RRAT J0139+3336 is affected by diffractive scintillation. An examination of the dynamic spectrum shown in Figure 2 also confirms the occurrence of scintillation. The scintillation bandwidth can be estimated from the autocorrelation function (ACF) of the single-pulse intensity in different frequency channels (Cordes et al. 2004):

$$A(\delta\nu) = \langle I(\nu) I(\nu + \delta\nu) \rangle; \quad (2)$$

$\delta\nu$ is the frequency lag of one channel shift for each pulse. Each $A(\delta\nu)$ is fitted by a Gaussian function. The standard deviation, σ, obtained from the fitting is used to derive the scintillation bandwidth, calculated as $\nu_{\mathrm{sc}} = (2\ln 2)^{1/2}\sigma$, which is the corresponding half-width at half-maximum of the Gaussian. Figure 3 shows the ACFs and best-fit Gaussian functions with the subset of 30 bright single pulses with S/N > 60, which can be applied to estimate the scintillation bandwidth. We obtained an average scintillation bandwidth $\nu_{\mathrm{sc}} = 28$ MHz at 1.25 GHz. The statistical uncertainty σ_{sc} in the scintillation bandwidth is given by Bhat et al. (1999)

$$\sigma_{\mathrm{sc}} = \left[\left(\frac{B_{\mathrm{obs}}}{\nu_{\mathrm{sc}}}\right) f_d\right]^{-1/2} \quad (3)$$

where B_{obs} is the observation bandwidth, and f_d is the filling fraction for a number of scintles, which is assumed to be 0.5. Note that 0.5 is a moderate value and may overestimate the number of scintles within the observed bandwidth if the typical separation between the scintles is much larger than their size. Finally, the scintillation bandwidth calculated by the above method is 28 ± 9 MHz at 1.25 GHz.

[7] https://www.scipy.org/

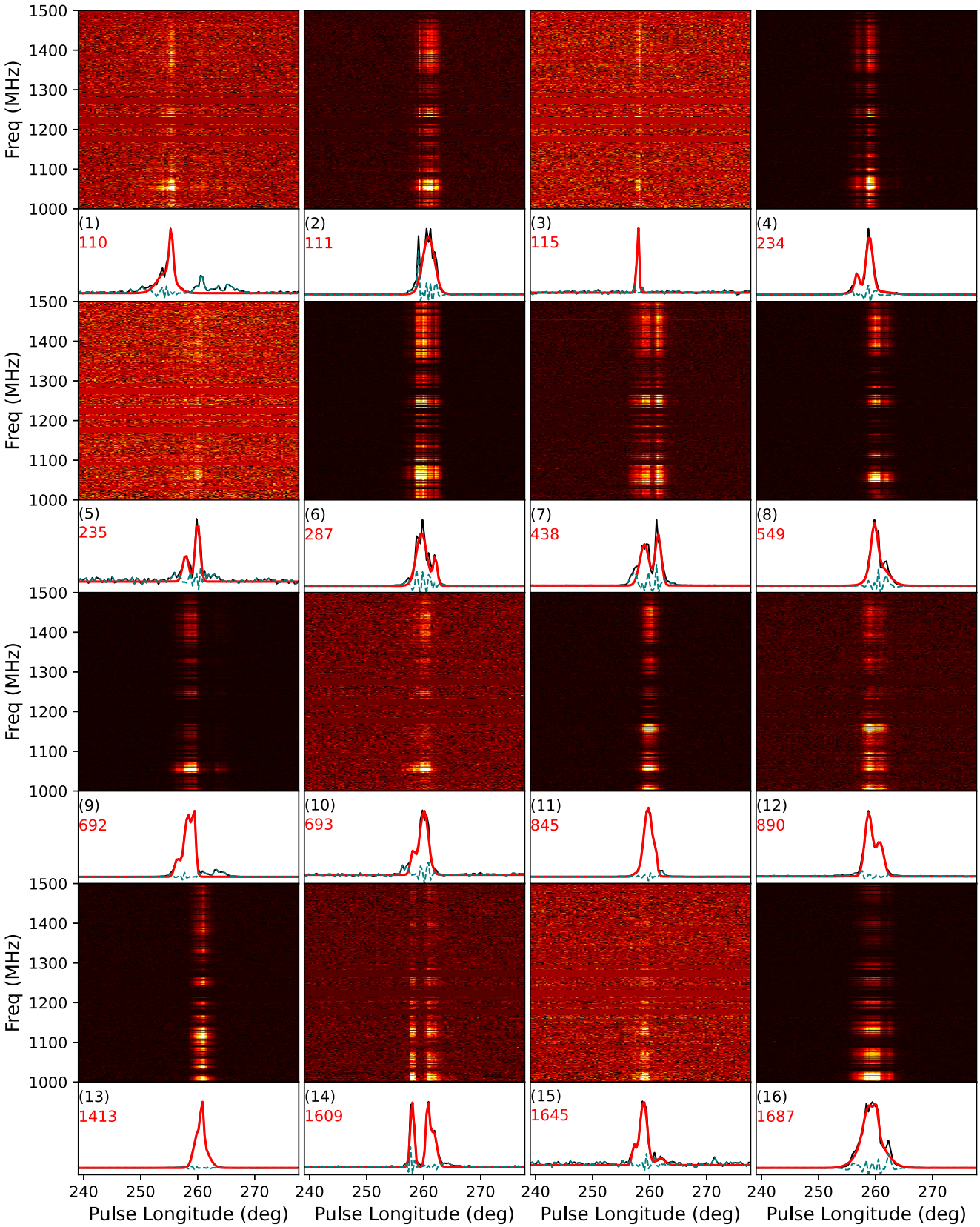

Figure 1. Sample of single pulses of RRAT J0139+3336. The dedispersed frequency-time plot for the single pulse is displayed in the top panel. The black line in the bottom panel of each plot shows the pulse profile after accumulating the frequencies, and the red line is the fitted multi-Gaussian Gaussian template. The green dashed line indicates the difference between the fitted line and the observed profile. Red numbers are the index of single pulses.

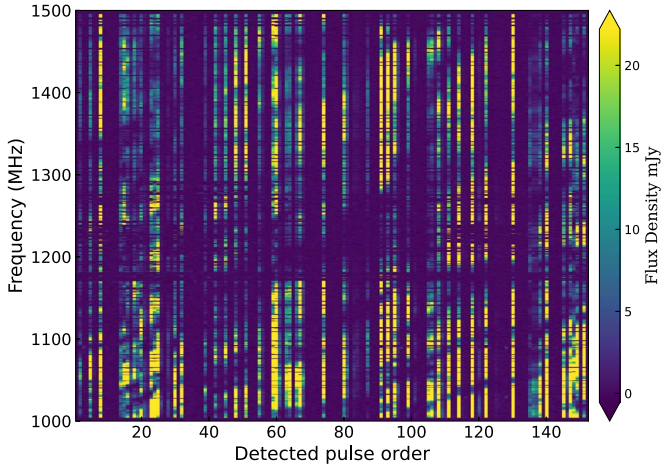

Figure 2. A dynamic spectrum of the single pulses from RRAT J0139+3336 at 1.25 GHz.

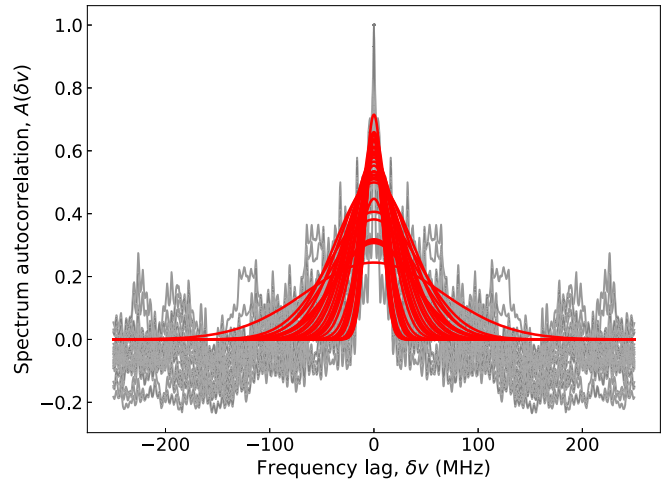

Figure 3. The solid gray line indicates the ACF of the dynamic spectrum with signal-to-noise ratios above 60 at the observed frequency, and the solid red line is their best-fit Gaussian model.

3.2. Spectral Indices

It is necessary to obtain the flux density of the pulses in each subband in order to fit a spectral index to every single pulse. The bandwidth was split into eight subbands.

The pulse widths across different subbands are only slightly different. Therefore, we assume the on-pulse region is constant across different subbands and define it as four times W50. Then Equation (1) is used to obtain the width of every single pulse. The mean measured W50 and W10 (the width of the pulse at 50 and 10 percent of its peak value) are 5.72 ± 0.15 ms and 13.4 ± 0.15 ms, respectively.

The flux density, S, and error, e, for a subband can be measured as follows (Kumamoto et al. 2021)

$$S = (\sum_{i=1}^{N_{\rm on}} I_i)/N_{\rm tot} \quad \text{and} \quad e = \sigma\sqrt{N_{\rm on}}/N_{\rm tot}, \tag{4}$$

where $N_{\rm on}$ is the number of phase bins across the on-pulse region, I_i is the intensity in ith bin, $N_{\rm tot}$ is the total number of phase bins per period, σ is the rms of the off-pulse.

It is assumed that the relationship between the flux density and the observed frequency follows a simple power-law function

$$S_\nu = bx^\alpha, \tag{5}$$

where S_ν is flux density at subband center frequency ν, $x = \frac{\nu}{\nu_0}$, $\nu_0 = 1.3$ GHz is a constant reference frequency, α is the spectral index, and b is a constant. A spectral index was calculated for every single pulse using its measured flux density for each subband. Several examples of fitted single-pulse spectral indices are shown in Figure 4. The distribution of spectral indices for all identified single pulses is shown in Figure 5. The spectral indices of the single pulses follow a normal distribution. The mean spectral index for our obtained single pulses is -3.2 ± 0.2, which is steep compared to a mean spectral index of large pulsar samples (see, e.g., Lorimer et al. 1995; Maron et al. 2000; Jankowski et al. 2018). Jankowski et al. (2018) reported a mean of -1.60 ± 0.54 in a study of 278 pulsars. The mean spectral indices that we measured for RRAT J0139+3336 appear to be similar to the results reported by Meyers et al. (2019) for the spectral indices of RRAT J2325-0530, but slightly steeper. Note that we only have L-band data, while Meyers et al. (2019) used two-band wide-band data extended to low frequencies. So it is a different part of the spectrum. The measurement of the spectral index of a single pulse has an extensive range ($-11.85 \leqslant \alpha \leqslant 3.83$).

3.3. Polarization Analysis

Accumulating the detected single pulses, we obtained the pseudointegrated pulse profile and the polarization profile, as shown in Figure 6. The profiles have been corrected for Faraday rotation, removing the effects induced by the ionosphere and the interstellar medium. To calculate the bias-corrected value of linear polarization, we followed a method described in Wardle & Kronberg (1974). The pseudointegrated profile is moderately linearly polarized with a fractional linear polarization of 34.3%. The position angle (PA) curve of the linear polarization is shown in the upper panel of Figure 6. The curve shows the characteristic S-shaped swing. The magnetic inclination angle α and impact parameter β can be used to determine the emission geometry of a pulsar. To constrain these parameters, we fitted the PA variation of the integrated profile as a function of pulse longitude with the rotating vector mode (RVM; Radhakrishnan & Cooke 1969):

$$\tan(\psi + \psi_0) = \frac{\sin\alpha\sin(\phi - \phi_0)}{\sin\zeta\cos\alpha - \cos\zeta\sin\alpha\cos(\phi - \psi_0)}, \tag{6}$$

where ψ is the PA at a pulse longitude ϕ, ψ_0 and ϕ_0 are the phase offsets for polarization position angle and pulse rotational phase, respectively, α is the angle between the rotation axis and the magnetic axis, and ζ is the angle between the positive spin axis and the pulsar-observer line of sight (LOS). The combined polarization position angle traverse was fitted to Equation (6) (shown as a solid green line in Figure 6). As can be seen from Figure 6, the position angle variation can be fitted well by the RVM, but the parameters cannot be well constrained based on reduced chi-squared χ^2. The only conclusion we can draw is that the angle between the magnetic axis and the observer's LOS $\beta < 4°$. According to Rookyard et al. (2015), further constraints on the viewing geometry can be obtained. The pulse width of RRAT J0139+3336 is relatively narrow (W10 $\approx 7.^\circ0 \pm 0.^\circ35$),

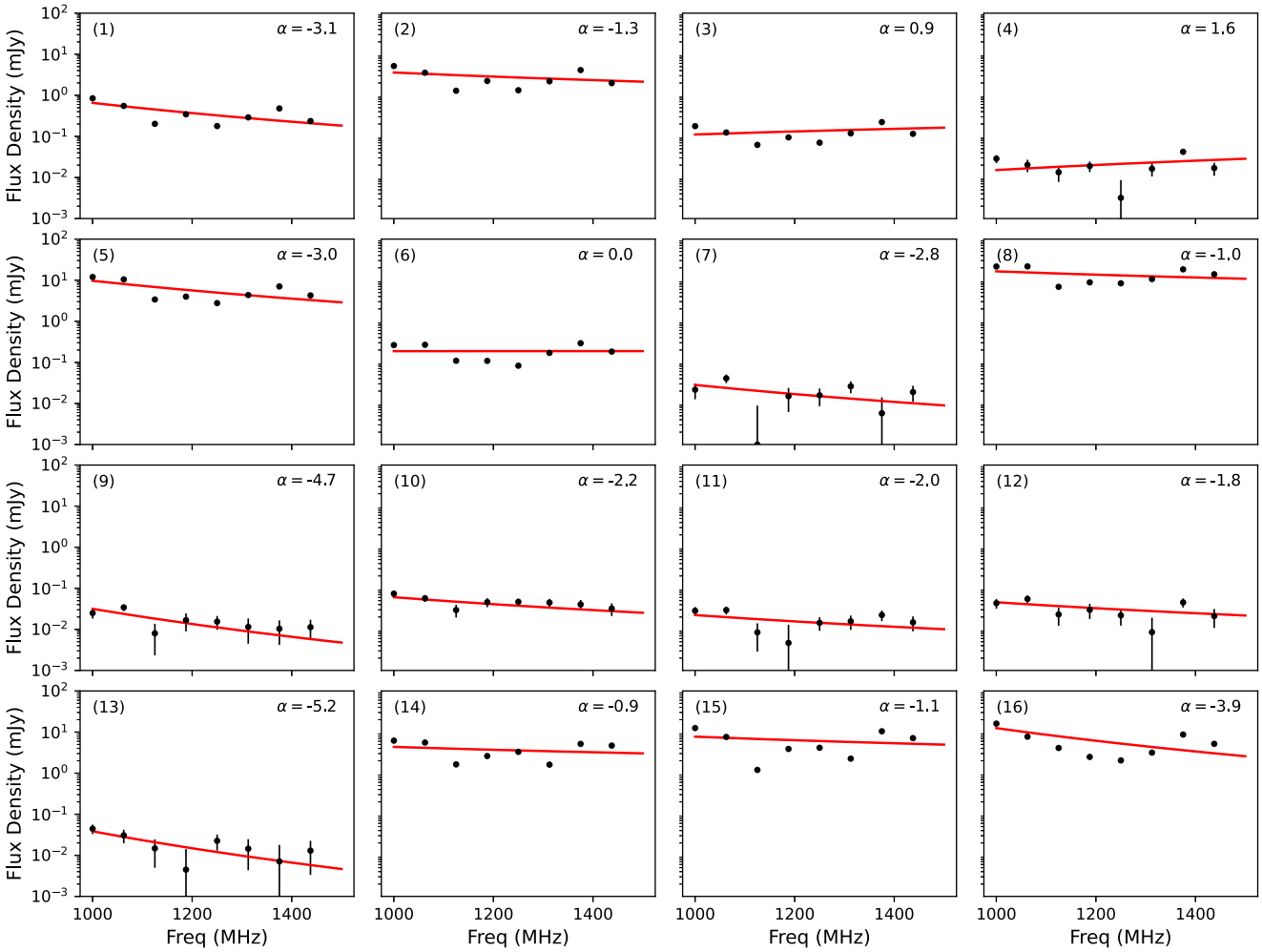

Figure 4. Fitting a sample of single-pulse spectral indices for RRAT J0139+3336. The spectral index fit for each single pulse corresponds to the single pulse in Figure 1. Each pulse spectral index fit has the same frequency and flux density scales. The scaled mean flux density is obtained from Equation (5) and is plotted against frequency in logarithmic space.

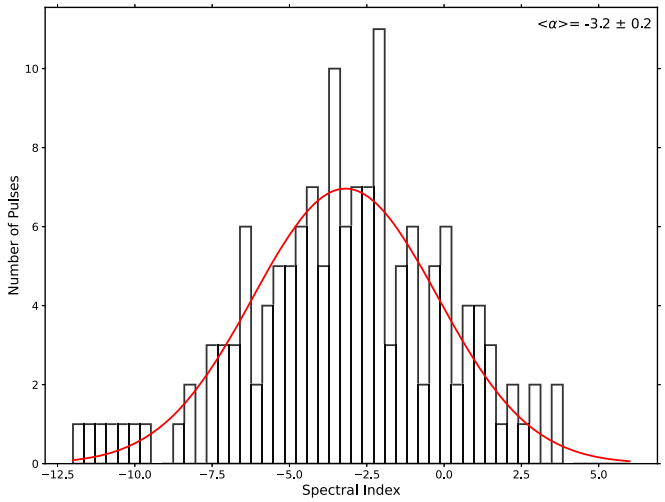

Figure 5. The distribution of 152 single-pulse spectral indices for RRAT J0139+3336.

which implies that either the emission comes from low in the magnetosphere or α is large. The inflection point will be delayed relative to the position of the fiducial plane. The upper limit of this delay $\Delta\phi$ for our observation is $\sim 0.^{\circ}32$, the emission height was given by

$$h_{\rm em} = \frac{\Delta\phi P c}{8\pi}, \tag{7}$$

where P is the rotation period of RRAT J0139+3336 and c is the speed of light (Blaskiewicz et al. 1991). The results calculated from the above method imply an emission height lower than 85 ± 10 km. We have identified values of α and β that can produce a pulse with measured width. These are shown as green areas in the right panel of Figure 6 and indicate that the magnetic axis is relatively aligned with the pulsars rotation axis with $\alpha < 50^{\circ}$.

3.4. Pulse Energy Distribution

With each single pulse calibrated, an analysis of the pulse energy distribution was carried out using the total flux density of each pulse. In order to compare with the results from Cui et al. (2017), we also construct pulse amplitude (the peak flux density) distributions.

The pulse energy and amplitude distributions for all detected single pulses are displayed in Figure 7. The distribution of pulse energy is similar to the distribution of pulse amplitude. To these distributions, we fit five relativity common models using the

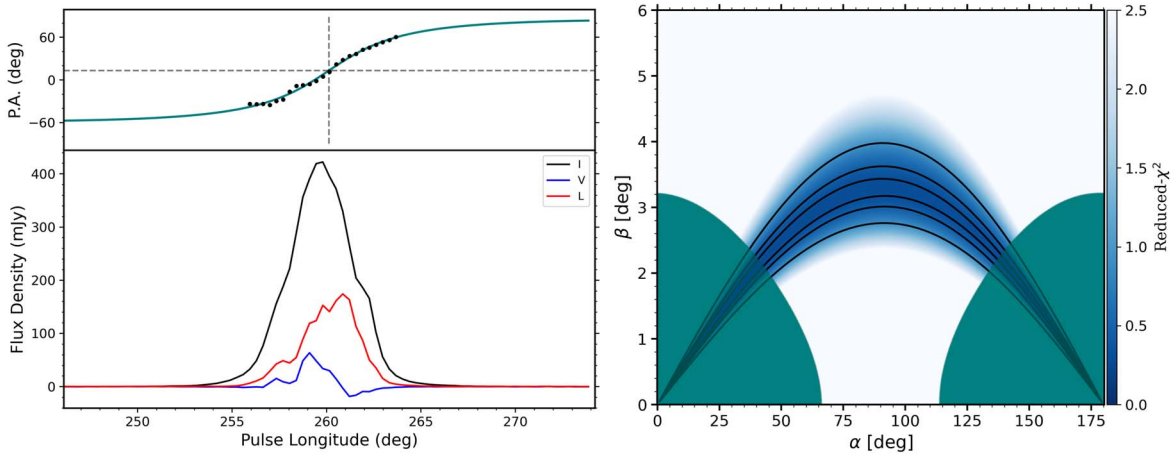

Figure 6. Left: the polarization profile at 1.25 GHz, including total intensity (black curve), linear polarization (red curve), and circular polarization (blue curve). Upper panel shows the linear polarization position angle in degrees, and green curve represents the fitting result using RVM model. Right: the results of fitting an RVM curve for each (α, β) combination. The reduced chi-squared of the fit is expressed in terms of color depth, with darker blue values corresponding to a better fit. The black contours correspond to $1\sigma-$, $2\sigma-$, and 3σ confidence boundaries. The green areas indicate the constraints given according to certain theoretical assumptions and observed parameters.

Python SCIPY module: a pure Weibull, log-normal, gamma, power-law, and exponential distribution as described in Meyers et al. (2019). The log-normal can well fit the energy and amplitude distribution. To quantify the fit, the Kolmogorov–Smirnov statistics (K-S test) of the sample versus its log-normal fit is performed, as shown in Figure 7. The obtained p value is greater than the threshold value of 0.05, which indicates that the observed distribution is consistent with a log-normal distribution. The p value is $<1\%$, and the null hypotheses for the other four distribution models (where the two distributions are the same) is rejected. It is further notable that the power-law model is only applicable to the pulses that have pulse energies greater than 0.002 $\langle E \rangle$. The cutoff was chosen to coincide roughly with the peak of the distribution. Without restriction, the power-law model fits the data poorly. The band-integrated peak flux density has a median value of 47.77 mJy and a standard deviation of 523.56. The band-integrated energy density has a median value of 421.34 mJy and a standard deviation of 7922.60.

3.5. Pulse Rate and Wait Time

In total, we acquired 152 pulses with a signal-to-noise ratio greater than six with FAST. These detections correspond to pulse rates of $45 \pm 3\,\mathrm{hr}^{-1}$ above a peak flux density of 3.59 mJy at 1.25 GHz, where the uncertainties correspond to the Poisson counting error. The previously published pulse rate is 12 pulses per hour with the LOFAR and Lovell at 149 and 1532 MHz (Michilli et al. 2020), respectively, which is about $1/4$ of what we measured.

In addition, an investigation of the distribution of the number of rotations between subsequent single pulses ("wait times") was carried out using our observations. To reduce the influence of artificial effects, a total of 112 pulses with a signal-to-noise ratio greater than 10 were selected as samples for analysis. The wait times will be exponentially distributed if the single-pulse emission is produced by a Poisson process. The distribution of wait times is shown in Figure 8 and an exponential distribution has been fitted to the wait times and the fitting parameters are shown in Table 2. The median and mean wait times are 82 and 124 rotations, respectively. The maximum wait time is 1265 rotations (i.e., ∼1578 s). With a sensitivity limit of $S/N \geqslant 10$, there were 31 wait times more than 100 rotations. There were

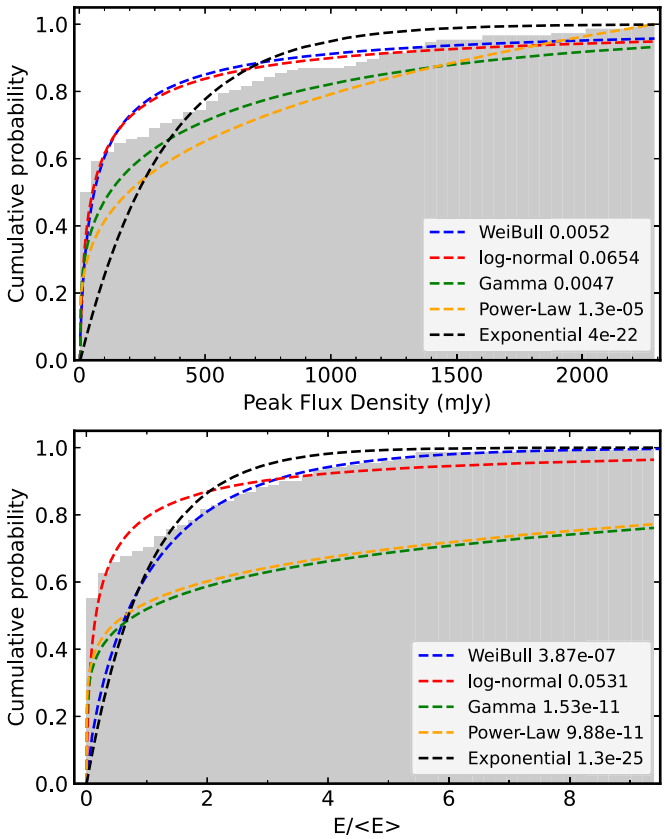

Figure 7. Normalized cumulative distribution of pulse peak flux (upper panel) and the energy (the lower panel) for single pulses detected. The best-fit log-normal is shown in the red dashed curve. In addition we fit the distribution with a pure Weibull (blue), gamma (green), power law (orange), and exponential (black), respectively, which cannot describe the observed distribution well. The numbers in the legend are the p values corresponding to the fitted distributions.

28 zero wait times with emission for two rotations and one zero wait time with emission for three rotations, which is consistent with exponential distribution. It is also significant to note that these numbers are likely to be affected by telescope sensitivity and threshold settings.

Table 2
Best-fit Parameters for Peak Fluence, Energy, and Wait-time Distribution Models

Parameter (MHz)	Power Law		Log-normal		
	β	χ_r^2	μ (mJy)	σ (mJy)	χ_r^2
Peak fluence	0.71 ± 0.02	1.20	3.88 ± 2.62	2.36 ± 0.91	1.16
Energy	0.48 ± 0.02	2.29	6.60 ± 1.77	2.29 ± 0.47	1.78
Wait Time	0.009 ± 0.001	1.006	…	…	…

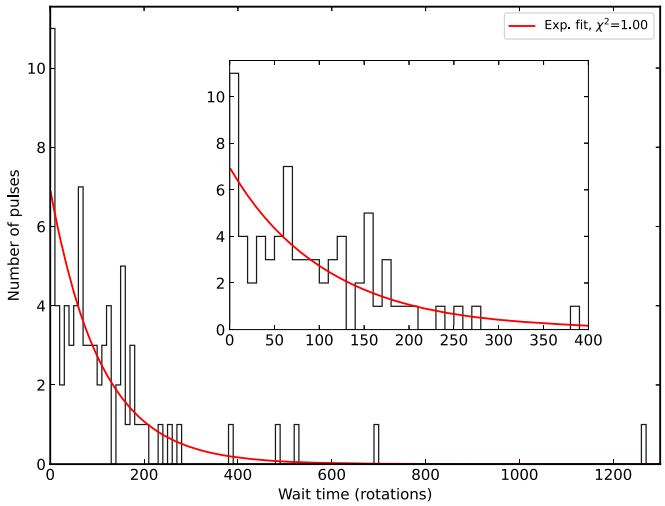

Figure 8. Histogram of the distribution of interval pulses between subsequent pulses; the solid red line is the result of fitting with an exponential distribution.

4. Discussion and Conclusions

4.1. Spectral Index

The single-pulse spectral index distribution of RRATs has not been well explored due to limitations in pulsar luminosity and radio telescope sensitivity. Recently, Meyers et al. (2019) and Shapiro-Albert et al. (2018) provided spectral index measurements for four RRATs (J1317-5759, J1819-1458, J1913+1313, and J2325-0530) and revealed that their mean spectral indexes do not differ significantly from the normal pulsar population distribution. Our measurement is also consistent with these. However, as studies of the spectral indices of RRATs remain scarce and limited by the low burst rate of RRATs, the mean spectral indices of RRATs are still poorly explored and no clear picture has emerged yet. As shown in Figure 4, there is a vast amount of pulse-to-pulse variations in the measured single-pulse spectral indices, with a discrepancy of ∼16 between the highest and lowest values we found as shown in Figure 5. Shapiro-Albert et al. (2018) also demonstrate the wide spread of the spectral indices of RRATs. A wide range of single-pulse spectral indices may be attributed to the intrinsic emission process or to the fact that the spectral indices were measured within the limited observing bandwidth. It is known that there is a significant difference in the spectral index distribution between normal pulsars and giant pulses from the Crab pulsar (Karuppusamy et al. 2010). And the difference between the minimum and maximum values of the spectral indices of giant pulses is up to 25. Therefore, it is not surprising that this is also true for RRATs.

The presence of scintillation is clearly seen by dynamic spectral examination, and the scintillation bandwidth is calculated by ACF to be 28 ± 9 MHz. For narrower subbands, the flux is entirely affected by scintillation for the RRAT single pulses, which is reflected in the change in spectral index we measured. It is significantly better quenched with the wider subbands. However, diffractive scintillation is not fully averaged out in our data, even with 62 MHz subbands. Therefore, spectral indexes in this Letter are still affected by diffractive scintillation. As such, it is challenging to estimate the flux density and spectral index of RRATs with low DM due to scintillation. To investigate the effect of scintillation on the spectral index of the single pulse, we calculated the spectral index for a subband of 16 MHz and obtained an average value of −2.4, which is significantly larger than the spectral index obtained with a bandwidth of 62. In the case of 16 MHz subbands, it is most likely diffractive scintillation that skews our data.

4.2. Pulse Energy

It is difficult to establish a robust model for the distribution of pulse energy with a limited number of single pulses. As described in Section 3.4, the power-law models only afford a reasonable fit to pulses above an arbitrary pulse energy cutoff. To describe the pulse energy distribution, any model should be able to take into account both high-energy and low-energy pulses, which the power law is incapable of doing. The energy distribution was fitted with different models and the results of the fit were tested using the reduced chi-squared statistics χ^2 tests, which showed that the log-normal model was a better fit. Furthermore, the log-normal is a better model through comparison of the K-S test. Brylyakova & Tyul'bashev (2021) concluded that the energy distribution of RRAT J0139+3336 can be described by a broken power-law model at 111 MHz. Some recent works suggest that the energies of RRATs follow a log-normal distribution (see, e.g., Cui et al. 2017; Shapiro-Albert et al. 2018; Meyers et al. 2019), and this appears to be the case for RRAT J0139+3336. The difference in pulse energy distribution may indicate the existence of a frequency evolution in RRAT J0139+3336. Such an evolution has been seen in other pulsars (Young et al. 2014). Therefore, it is not surprising if frequency evolution of pulse energy distribution is seen in RRAT. Alternatively, due to the limited number of observed pulses, it is not strictly certain that the energy of RRAT J0139+3336 follows the log-normal distribution.

Singal & Vats (2012) defined giant pulses as very bright single pulses with an energy greater than 10 times the average pulse energy. Some studies in recent years have shown that giant pulses are characterized by their power-law energy distribution (McKee et al. 2019; Sun et al. 2021). Brylyakova & Tyul'bashev (2021) reported that RRAT J0139+3336 is a rotating transient with giant pulses. In our observation, we did not find any pulses exceeding 10 times the average energy of all detected pulses.

Table 3
Pulse Rates and Nominal Detection Sensitivity for Single Pulses from RRAT

Telescope	Frequency (MHz)	Bandwidth (MHz)	Pulse Rate (hr^{-1})	References
LOFAR	149	78	~12	Michilli et al. (2020)
Lovell	1532	384	~12	Michilli et al. (2020)
FAST	1250	500	45 ± 3	This work

4.3. Pulse Rates and Wait Time

On the basis of the known pulse rates of RRATs[8], there are ~90% of RRATs with pulse rates below 100 pulses per hour and 25 rotating radio transients with pulse rates above RRAT J0139+3336. For RRAT J0139+1336, the previously published pulse rate is 12 pulses per hour at 150 MHz and 1552 MHz (see Table 3 for details). Our measured pulse rate from the FAST data is much higher than that of LOFAR and Lovell. The observing frequency of FAST and Lovell are very close, but the sensitivity of FAST is much higher than that measured with the Lovell Telescope. This could possibly imply that the burst rate of RRAT J0139+1336 depends on the radio telescope sensitivity. Note that comparing pulse rates between different observing epochs intrinsically assumes that the pulses are generated by a Poisson process, where pulses occur at a constant average rate and independently. It is not clear whether this is the case for RRATs in general. The waiting times can be fitted by an exponential distribution, similar to the case of other RRATs (see, e.g., Meyers et al. 2019; Chen et al. 2022). Due to a limited number of single-pulse detections, it is not clear whether there is a significant deviation from the expected pulse events drawn from a Poisson process.

4.4. Conclusion

We present a single-pulse analysis of RRAT J0139+3336 at 1250 MHz based on observation from the FAST radio telescope. Over the observation, we detected 152 pulses, implying a pulse rate of $45 \pm 3\ \mathrm{hr}^{-1}$ which is much higher than previous results. We estimated the RM for this RRAT, with $\mathrm{RM_{ISM}} = 38.61 \pm 0.32\ \mathrm{rad\ m^{-2}}$. The single-pulse spectral indices of RRAT J0139+3336 are normally distributed around a mean spectral index, which is relatively steeper compared to the normal pulsar population. Scintillation at 1.25 GHz is clearly seen with a characteristic scintillation bandwidth of $\nu_{\mathrm{sc}} = 28 \pm 9$ MHz. The polarization of RRAT J0139+3336 is similar to that of the normal pulsar population. The linear polarization position angle traverse tracks of RRAT J0139+3336 show the characteristic S-shaped curve, which can be well fitted using the rotating vector model. The single-pulse energy distribution of RRAT J0139+3336 can be described by either a log-normal or a power-law model, which is in agreement with previous RRAT studies.

This work is supported by the National Natural Science Foundation of China (No. 12041304), the National SKA Program of China (No. 2020SKA0120100), the 201* Project of Xinjiang Uygur Autonomous Region of China for Flexibly Fetching in Upscale Talents, the CAS Jianzhihua project, the Operation, Maintenance, and Upgrading Fund for Astronomical Telescopes and Facility Instruments, budgeted from the Ministry of Finance of China (MOF) and administrated by the Chinese Academy of Science (CAS). This work drew on data from FAST, China's national large-scale scientific facility operated by the National Astronomical Observatory of the Chinese Academy of Sciences.

[8] http://astro.phys.wvu.edu/rratalog/

Data Availability

The observations used in this Letter can be shared with the corresponding author if there is a reasonable demand.

ORCID iDs

Jintao Xie https://orcid.org/0000-0001-5649-2591
Jingbo Wang https://orcid.org/0000-0001-9782-1603
Na Wang https://orcid.org/0000-0002-9786-8548
Feifei Kou https://orcid.org/0000-0002-0069-831X
Shuangqiang Wang https://orcid.org/0000-0003-4498-6070

References

Baars, J. W. M., Genzel, R., Pauliny-Toth, I. I. K., & Witzel, A. 1977, A&A, 500, 135
Bhat, N. D. R., Rao, A. P., & Gupta, Y. 1999, ApJS, 121, 483
Blaskiewicz, M., Cordes, J. M., & Wasserman, I. 1991, ApJ, 370, 643
Brylyakova, E. A., & Tyul'bashev, S. A. 2021, A&A, 647, A191
Burke-Spolaor, S., & Bailes, M. 2010, MNRAS, 402, 855
Burke-Spolaor, S., Johnston, S., Bailes, M., et al. 2012, MNRAS, 423, 1351
Chen, J. L., Wen, Z. G., Yuan, J. P., et al. 2022, ApJ, 934, 24
Cordes, J. M., Bhat, N. D. R., Hankins, T. H., McLaughlin, M. A., & Kern, J. 2004, ApJ, 612, 375
Cordes, J. M., & Shannon, R. M. 2008, ApJ, 682, 1152
Cui, B. Y., Boyles, J., McLaughlin, M. A., & Palliyaguru, N. 2017, ApJ, 840, 5
Feng, Y., Hobbs, G., Li, D., et al. 2021, ApJ, 908, 105
Hotan, A. W., van Straten, W., & Manchester, R. N. 2004, PASA, 21, 302
Jankowski, F., van Straten, W., Keane, E. F., et al. 2018, MNRAS, 473, 4436
Jiang, P., Tang, N.-Y., Hou, L.-G., et al. 2020, RAA, 20, 064
Karuppusamy, R., Stappers, B. W., & van Straten, W. 2010, A&A, 515, A36
Kumamoto, H., Dai, S., Johnston, S., et al. 2021, MNRAS, 501, 4490
Li, X.-D. 2006, ApJL, 646, L139
Liu, B., & Yu, S. 2020, in Big Data in Astronomy: Scientific Data Processing for Advanced Radio Telescopes, ed. L. Kong et al. (Netherlands: Elsevier), 165
Lorimer, D. R., Yates, J. A., Lyne, A. G., & Gould, D. M. 1995, MNRAS, 273, 411
Maron, O., Kijak, J., Kramer, M., & Wielebinski, R. 2000, A&AS, 147, 195
McKee, J. W., Stappers, B. W., Bassa, C. G., et al. 2019, MNRAS, 483, 4784
McLaughlin, M. A., Lyne, A. G., Keane, E. F., et al. 2009, MNRAS, 400, 1431
McLaughlin, M. A., Lyne, A. G., Lorimer, D. R., et al. 2006, Natur, 439, 817
Melrose, D. B., & Yuen, R. 2014, MNRAS, 437, 262
Meyers, B. W., Tremblay, S. E., Bhat, N. D. R., et al. 2019, PASA, 36, e034
Michilli, D., Bassa, C., Cooper, S., et al. 2020, MNRAS, 491, 725
Radhakrishnan, V., & Cooke, D. J. 1969, ApL, 3, 225
Rookyard, S. C., Weltevrede, P., & Johnston, S. 2015, MNRAS, 446, 3356
Samodurov, V., Pozanenko, A., Rodin, A., et al. 2017, in International Conference on Data Analytics and Management in Data Intensive Domains, Observations of Transient Phenomena in BSA RadioSurvey at 110 MHz, 706 (Berlin: Springer), 130
Sanidas, S., Cooper, S., Bassa, C. G., et al. 2019, A&A, 626, A104
Shapiro-Albert, B. J., McLaughlin, M. A., & Keane, E. F. 2018, ApJ, 866, 152
Singal, A. K., & Vats, H. O. 2012, AJ, 144, 155
Sotomayor-Beltran, C., Sobey, C., Hessels, J. W. T., et al. 2013, A&A, 552, A58
Sun, S. N., Yan, W. M., & Wang, N. 2021, MNRAS, 501, 3900
Timokhin, A. N. 2010, MNRAS, 408, L41
Tyul'bashev, S. A., Tyul'bashev, V. S., Malofeev, V. M., et al. 2018, ARep, 62, 63
van Straten, W., & Bailes, M. 2011, PASA, 28, 1
Wang, N., Manchester, R. N., & Johnston, S. 2007, MNRAS, 377, 1383
Wardle, J. F. C., & Kronberg, P. P. 1974, ApJ, 194, 249
Young, N. J., Weltevrede, P., Stappers, B. W., Lyne, A. G., & Kramer, M. 2014, MNRAS, 442, 2519